Journal of Solid State Chemistry 182 (2009) 115–121

Contents lists available at ScienceDirect

Journal of Solid State Chemistry

journal homepage: www.elsevier.com/locate/jssc

Shape-controlled fabrication of porous ZnO architectures and their photocatalytic properties

Jun Zheng, Zhi-Yuan Jiang *, Qin Kuang *, Zhao-Xiong Xie, Rong-Bin Huang, Lan-Sun Zheng

State Key Laboratory for Physical Chemistry of Solid Surfaces and Department of Chemistry, College of Chemistry and Chemical Engineering, Xiamen University, Xiamen 361005, PR China

ARTICLE INFO

Article history:
Received 18 June 2008
Received in revised form
4 October 2008
Accepted 8 October 2008
Available online 19 October 2008

Keywords:
ZnO
Porous structures
Photodegradation

ABSTRACT

In this paper, we report a simple two-step approach to prepare porous octahedron- and rod-shaped ZnO architectures. The morphology of porous ZnO particles can be conveniently tuned by controlling morphologies of the $ZnC_2O_4 \cdot 2H_2O$ precursor. SEM and TEM characterization results indicate that these porous ZnO architectures are built up by numerous ZnO primary nanoparticles with random attachment. Based on thermogravimetry analysis, we believe that the release of water vapor, CO and CO_2 leads to the formation of high-density pores in shape-controlled particles during the calcination process. Further experimental results indicate that as-prepared porous ZnO particles exhibit good photocatalytic activity due to large surface area.

1. Introduction

Due to large surface area, high porosity and low density, porous materials have practical applications in many fields, ranging from bioengineering, catalysis, separation, and environmental engineering to chemical and gas sensors [1–4]. Up to now, kinds of methods, such as hard templates [5,6], soft templates [7,8], directional freezing [9], ultrasonic spray pyrolysis [10] and so on, have been explored to fabricate various materials with porous structures. Recently, morphology-controlled syntheses of porous materials are gaining more and more attention because porous materials of different macroscopic morphology are found to present different properties, which greatly affect their practical applications [7,11–18]. For example, spherical porous particles and capsules have superiority in applications for drug delivery and release [4,14] whereas one-dimensional porous nanostructures (i.e., nanowires and nanotubes) in comparison are more suitable for optoelectronic nanodevices, such as sensors [16,17]. In a recent literature [18], Dai and co-workers demonstrated that porous ZnO particles with a tetragonal pyramid shape have better biosensing properties than spherical ZnO nanoparticles. Except silica-based porous materials [11–14], however, there are few successful cases about precise and tunable control over the morphology of porous materials. For this reason, to explore a simple strategy for morphology-controlled synthesis of porous materials is still a significant challenge for modern synthetic science.

Zinc oxide (ZnO), a remarkable II–VI semiconductor with a direct wide band gap of 3.37 eV and large exciton binding energy of 60 meV at room temperature, has attracted considerable interests due to potential applications in laser [19], solar cells [20], sensors [21,22], photocatalysts [23], etc. As a result of unique anisotropic features of wurtzite structure, ZnO is probably the richest family of nanostructures among all materials including carbon nanotubes [24]. Among diverse morphologies of ZnO, ZnO particles with a porous structure have attracted increasing attention in recent years since porous particles may present potential properties superior to corresponding solid structures. For example, porous ZnO nanotubes, which have been reported by Wang et al. [25], exhibit superior photocatalytic activity in the degradation of methyl orange compared to commercial ZnO powders, ZnO double layer microdisks, and even anatase TiO_2 nanoparticles. As far as we know, there are no successful cases at present for morphology-controlled synthesis of porous ZnO particles through a versatile strategy although various porous ZnO structures, including porous pyramids [18], porous nanotubes [25], mesoporous polyhedral cages [26], porous hexagonal disks [27–29], porous nanowires [30], and porous nanobelts [31–33], have successfully prepared by means of various methods.

In this paper, we report a simple approach to prepare porous ZnO particles with two kinds of regular morphologies, i.e., octahedron and nanorods. The morphology of as-prepared porous ZnO particles can be conveniently tuned by controlling morphologies of zinc oxalates as precursors. Based on thermogravimetric

* Corresponding authors. Fax: +86 592 2183047.
E-mail addresses: zyjiang@xmu.edu.cn (Z.-Y. Jiang), qkuang@xmu.edu.cn (Q. Kuang).

0022-4596/$ - see front matter © 2008 Elsevier Inc. All rights reserved.
doi:10.1016/j.jssc.2008.10.009

analysis, we proposed a rational mechanism for explaining evolution of porous ZnO particles with regular morphologies from the precursors to final products. Photocatalytic activity of as-prepared porous ZnO particles has also been evaluated by investigating degradation of methyl orange under UV irradiation.

2. Experimental section

2.1. Chemicals and synthesis

All the reagents used in experiments were of analytical grade, and used as received without further purification. Zinc chloride ($ZnCl_2$) was purchased from Shantou Xilong Chemical Co., Ltd. Sodium sulfate (Na_2SO_4), oxalic acid dihydrate ($H_2C_2O_4 \cdot 2H_2O$), *N*, *N*-dimethylformamide (DMF) and methyl orange (MO) were purchased from Sinopharm Chemical Reagent Co., Ltd. The synthetic procedure of porous ZnO particles involves two steps, i.e., solvothermal synthesis of precursors and sequent calcination at high temperature. A typical synthetic experiment was as follows: (1) 0.5 g of Na_2SO_4, 0.068 g of $ZnCl_2$ and 0.126 g of $H_2C_2O_4 \cdot 2H_2O$ were added to 5 mL of ethanol and 5 mL of DMF under magnetic stirring. Then the solution was transferred into a Teflon-lined stainless autoclave with a capacity of 25 mL. After being sealed, the autoclave was heated at 180 °C for 24 h and then was naturally cooled to room temperature. After the reaction was completed, a powder was collected from the solution by centrifugation, and rinsed with aether, ethanol and deionized water in sequence. (2) The as-prepared powder was calcined at 500 °C for 1 h under normal atmospheric conditions, and finally a white product was obtained.

In our experiments, porous ZnO architectures with octahedron- and nanorod-like shapes were obtained by simply changing molar ratio of reactants ($ZnCl_2/H_2C_2O_4 \cdot 2H_2O$) as well as their growth environment. Table 1 lists detailed synthetic conditions of two kinds of porous ZnO architectures.

2.2. Characterization

The products were characterized by X-ray diffraction (XRD, PANalytical X-Pert diffractometer with Cu-*K*α radiation), field emission scanning electron microscopy (FESEM, LEO1530) equipped with energy-dispersive spectrometer (EDS), and high resolution TEM (HRTEM, FEI Tecnai-F30 FEG) with an acceleration voltage of 300 kV. Thermogravimetry (TG) analysis was carried out on a NETZSCH TG 209 F1 analyzer under a nitrogen atmosphere at a heating rate of 10 °C min^{-1} from 30 to 600 °C. X-ray photoelectron spectroscopy (XPS) measurements were carried out on a scanning ESCA microprobe (PHI Quantum 2000) with Al *K*α radiation. The binding energy was calibrated with a C_{1s} photoelectron peak at 284.6 eV. UV–Vis spectra were recorded on a spectrophotometer (Shimadzu UV-2501 PC) at room temperature. Photoluminescence (PL) spectrum was measured at room temperature with a luminescence spectrometer (Hitachi F-4500) using a Xenon discharge lamp as the excitation light source, and excitation wavelength was 325 nm.

2.3. Photocatalytic activity measurements

Photocatalytic activity of as-prepared ZnO porous architectures was tested by decomposing MO in water under UV irradiation of a 300 W high-pressure Hg lamp (the strongest emission at 365 nm). The temperature of photocatalytic reaction was kept at about 25 °C. In a typical experiment, as-prepared porous ZnO particles (5 mg) as photocatalysts were added into a series of Pyrex glass vessels containing 5 mL of MO (10 mg L^{-1}) to obtain suspensions for degradation reaction. Prior to UV irradiation, the suspensions were stirred in the dark for 5 min to ensure an adsorption/desorption equilibrium of MO on surfaces of porous ZnO particles. After a given irradiation time, the suspensions were withdrawn, and centrifuged to remove the particles. The degradation process as a function of irradiation time was monitored by measuring the absorption of MO in the solution at 463 nm with UV–Vis absorption spectra.

3. Results and discussion

Fig. 1a shows a typical SEM image of the precursor in the case of porous ZnO octahedra (sample 1). From this image, it can be found that the precursor is composed of micro-particles with an octahedron shape, the average size of which is about 2 μm. As shown in corresponding XRD pattern (Fig. 1b), all diffraction peaks of the precursor can be indexed to $ZnC_2O_4 \cdot 2H_2O \cdot$ with a monoclinic structure (JCPDS No. 25-1029). Fig. 1c is a typical SEM image of final products after the calcination at 500 °C for 1 h, which shows that the final products still retain an octahedral morphology of the precursor. High-magnification SEM image (Fig. 1d) clearly shows that these octahedron-shaped particles are of porous structure, and are constructed with large numbers of nanoparticles with the size between 40 and 50 nm. Abundant pores were observed in the particles. The composition and phase of final products can be further determined by EDS spectrum and XRD pattern. The EDS spectrum (inset of Fig. 1c) indicates that these octahedron-shaped particles consist of Zn element and O element (the peak of Si originates from the Si substrate to support the sample). In the XRD pattern of the final products (Fig. 1e), all diffraction peaks agree well with ZnO of wurtzite structure (JCPDS No. 36-1451) and no peaks from other impurities are detected. In addition, a significant widening of the diffraction peaks is observed in the XRD pattern of the final products. According to Scherrer Equation, the mean size of primary nanoparticles constructing porous octahedra is calculated to be about 40 nm, consistent with the observed size in SEM image.

More structural information of as-prepared porous octahedra was provided by the TEM characterization. Fig. 1f is a typical TEM image, clearly showing that these porous octahedra are polycrystalline, and constructed with numerous nanoparticles. Sharp diffraction rings in corresponding selected-area electron diffraction (SEAD) pattern (inset of Fig. 1f) suggest that primary nanoparticles are randomly attached together, instead of following oriented attachment mechanism.

Fig. 2a shows a typical SEM image of the precursor obtained under synthetic conditions of sample 2, which clearly shows that the precursor is of a one-dimensional rod-like shape. The average

Table 1
A brief summary of synthetic conditions of porous ZnO particles with different morphologies

Sample no.	Morphology of the product	Morphology of the precursor	$ZnCl_2$	$H_2C_2O_4 \cdot 2H_2O$	Na_2SO_4	Solvents
1	Octahedron	Octahedron	0.068 g	0.126 g	0.5 g	5 mL ethanol, 5 mL DMF
2	Nanorod	Nanorod	0.272 g	0.126 g	0 g	10 mL ethanol

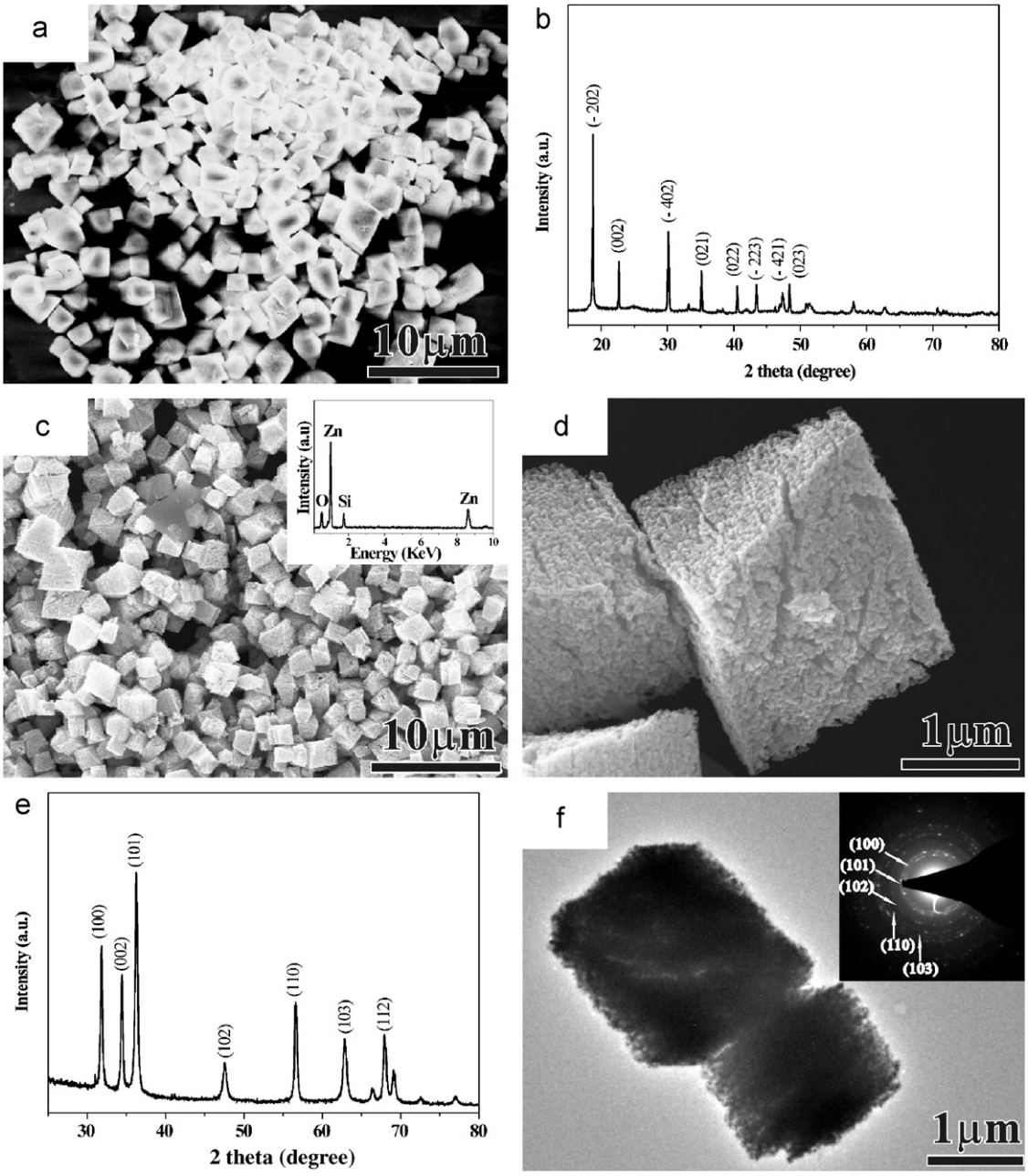

Fig. 1. (a) Low-magnification SEM image and (b) XRD pattern of the octahedron-like precursor; (c) low-magnification SEM image and (d) high-magnification SEM image of porous octahedra obtained by calcination at 500 °C. The inset is corresponding EDS spectrum; (e) XRD pattern of as-prepared porous ZnO octahedra; (f) TEM image of porous ZnO octahedra and corresponding SEAD pattern (the inset).

diameter of these rod-like precursors is about 200 nm, and the length is up to several micrometers. Corresponding XRD pattern (Fig. 2b) confirms that these nanorod-like precursors are also monoclinic $ZnC_2O_4 \cdot 2H_2O$. As shown in Fig. 2c, the whole morphology of final products after calcination still shows a rod-like shape, and the diameters are about 180 nm. According to high-magnification SEM image (Fig. 2d), these nanorods are built up by primary nanoparticles of 40–50 nm in size, and thus own numerous pores. Both corresponding EDS spectrum (inset of Fig. 2c) and XRD pattern (Fig. 2e) further indicate that these rod-like particles are pure ZnO. Similar with porous ZnO particles with octahedral shapes, as-prepared porous ZnO nanorods are also polycrystalline (see Fig. 2f).

In order to make clear the evolution process from the precursor (i.e., $ZnC_2O_4 \cdot 2H_2O$) to the final product (i.e., ZnO), thermal decomposition of the precursor was investigated by TG analysis. Fig. 3 is a TG curve of the octahedral precursor under a nitrogen atmosphere, showing the presence of two large weight loss stages. According to previous study [34], the first large stage of 20% weight loss at the range of 100–240 °C corresponds to the loss of two crystallization water of the precursor (i.e., $ZnC_2O_4 \cdot 2H_2O \rightarrow ZnC_2O_4$), and the second large stage of 38% weight loss at the range of 350–410 °C is ascribed to decomposition reaction of ZnC_2O_4 (i.e., $ZnC_2O_4 \rightarrow ZnO$). Total weight loss of 58% from the precursor to the final product is consistent with theoretical weight loss of the reaction from $ZnC_2O_4 \cdot 2H_2O$ to ZnO. Based on above TG analysis, a rational mechanism is proposed for explaining the formation of porous structures in ZnO architectures from the octahedral precursors through a calcination process. During the calcination process, the $ZnC_2O_4 \cdot 2H_2O$ precursors

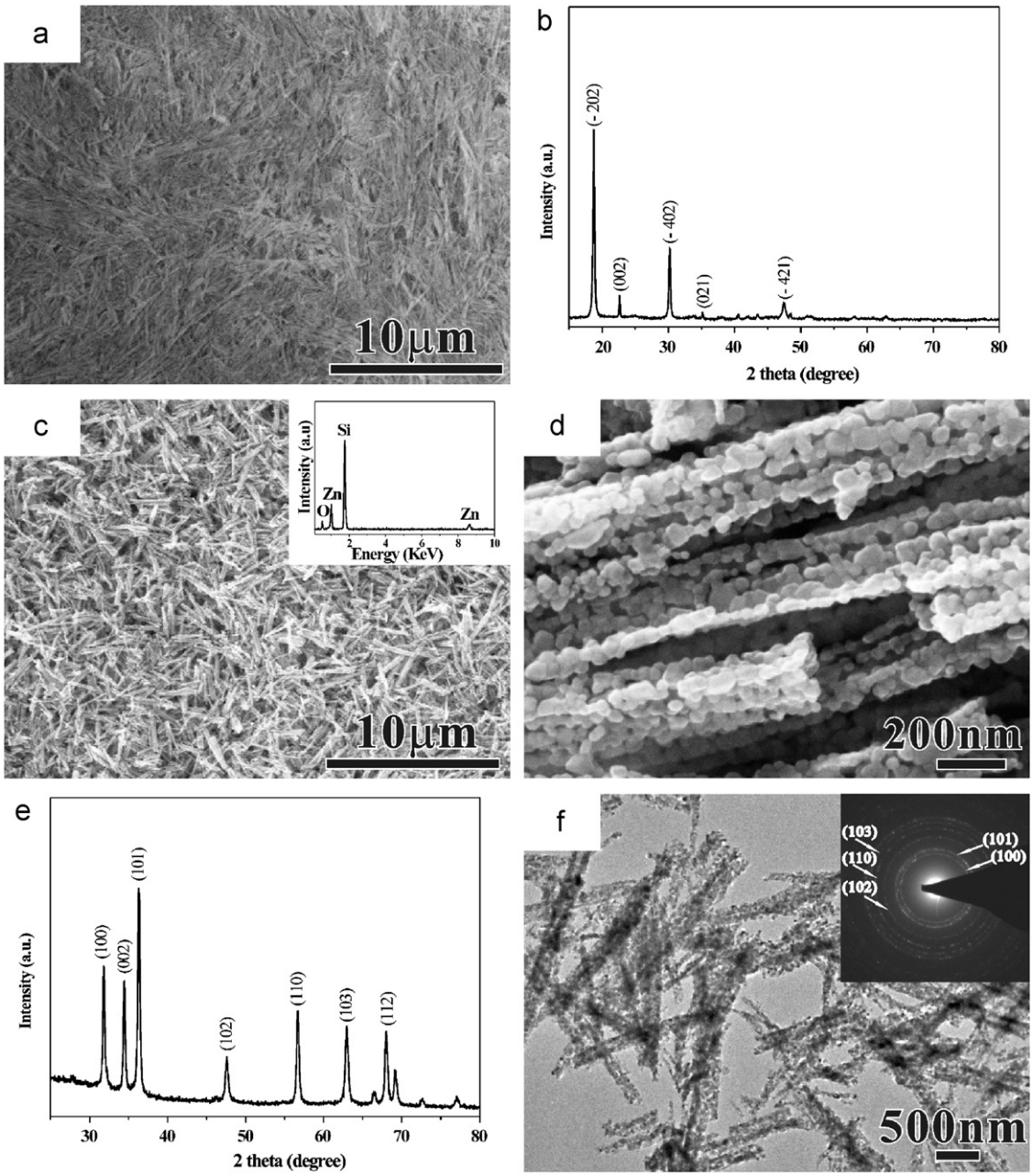

Fig. 2. (a) Low-magnification SEM image and (b) XRD pattern of the nanorod-like precursor; (c) low-magnification SEM image and (d) high-magnification SEM image of porous ZnO nanorods obtained by calcination at 500 °C. The inset is corresponding EDS spectrum; (e) XRD pattern of as-prepared porous ZnO nanorods; (f) TEM image of porous ZnO nanorods and corresponding SEAD pattern (the inset).

undergo dehydration and decomposition, and simultaneously release some gases including water vapor, CO and CO_2, which would lead to the formation of high-density pores in the precursor. Because nucleation and growth of ZnO primary particles uniformly occur in particles of the precursor, the whole particles are able to keep the same morphology as the precursor. Based on the above mechanism, thermal decomposition of $ZnC_2O_4 \cdot 2H_2O$ precursors is indeed an efficient way to obtain porous ZnO particles. Similar strategy has been successfully applied in the fabrication of porous NiO and MnO_x with a regular morphology [15].

Controlling morphology of the precursor is crucial for obtaining porous particles with a regular morphology. As is well known, growth environments severely affect surface energy and growth speed of crystal planes during the growth of nanocrystals, which accordingly determines final morphology of products. Recently, solvent-assisted syntheses under ionic conditions, such as ionic liquids [35,36] and molten salts [37], have become a kind of promising strategy for preparing nanoparticles with special morphologies. In our experiments, the presence of Na_2SO_4 in the solution also plays an important role in formation of octahedral precursors. No octahedral particles can be found in the precursor if it is without Na_2SO_4 in the solution during the hydrothermal process.

Calcination temperature is another key factor for controlling porous structure of as-prepared ZnO particles because sizes of nanoparticles prepared via thermal decomposition depends on decomposition temperature. Fig. 4a shows a typical SEM image of porous ZnO particles calcined at 700 °C, using the same ZnO octahedra as the precursor in sample 1. Although these particles

still keep an octahedral shape, the average size of ZnO primary nanoparticles constructing porous structures greatly increases up to 110 nm, and stacked more tightly when calcination temperature was raised to 700 °C from 500 °C.

ZnO is a kind of promising photocatalyst for dye degradation due to high photosensitivity and wide band gap of 3.37 eV [23,38–40]. Considering large surface area resulting from porous structures, as-prepared octahedron- and rod-like ZnO particles may exhibit good photocatalytic ability for dye degradation. Fig. 4b shows photodegradation curves of MO using three kinds of porous ZnO particles as photocatalysts. For all samples, photodegradation processes completed within 20 min. Porous ZnO octahedra calcined at 500 °C exhibit the best photocatalytic abilities whereas porous ZnO octahedra calcined at 700 °C is much slower in the photodegradation rate. The photocatalytic rate of porous ZnO nanorods calcined at 500 °C is in the middle of two different porous ZnO octahedra.

It is well known that photodegradation activity of photocatalysts has a close relation with their specific surface area, which determines the quantities of dye molecules adsorbed on the surface of photocatalysts. In our experiments, the diameters of primary nanoparticles constructing porous octahedra and nanorods obtained at 500 °C range from 40 to 50 nm. For the sample obtained at 700 °C, however, primary nanoparticles constructing porous structures became larger in size with increase in calcination temperature, up to about 110 nm. The increase in diameters of primary nanoparticles would inevitably reduce surface area of porous ZnO particles. As a result, porous ZnO particles obtained at relatively low calcination temperature of 500 °C have higher photocatalytic activities for MO degradation in comparison with porous ZnO octahedra calcined at 700 °C.

In addition, photocatalytic activities of metal oxides are closely related with surface structures of them. In our studies, XPS analysis was applied to acquire detailed information about surface structures of as-prepared porous ZnO particles. Fig. 5a and c show XPS spectra for the $Zn_{2p3/2}$ core level taken from samples 1 and 2. The binding energies are 1021.9 and 1022.0 eV, respectively. And XPS spectra for the O_{1s} core level are shown in Fig. 5b and d, respectively. For both samples, the peaks for O_{1s} center around 530.6 eV, and the peak profiles are asymmetric, a shoulder peak appearing at higher binding energy. XPS spectra for the O_{1s} core level suggest the presence of at least two different kinds of O species in the samples. According to previous study [41], the peak of O_{1s} around 530.6 eV should be indexed to lattice oxygen (O_L) of ZnO, and the shoulder peak at higher binding energy should be associated with O^{2-} ions in oxygen-deficient regions and chemisorbed and dissociated oxygen species on the surface of ZnO. The peak distributions of O_{1s} peaks for porous octahedra and nanorods are almost the same, suggesting that surface structures of them are similar to each other.

ZnO is also a kind of promising materials for short-wave laser and light emitting diode due to high exciton binding energy, intense stimulated emission, low lasing threshold, and high working temperature. Herein, PL spectrum was recorded to investigate luminescence properties of as-prepared porous ZnO particles. Fig. 6 shows a typical PL spectrum of porous ZnO octahedra measured at room temperature using the excitation wavelength of 325 nm. It can be found that a broadened peak around 400 nm was observed, which is attributed to the near band-edge emission of ZnO. In addition, a broadened blue–green emission peak is found around 450 nm, which is thought to be associated with structural defects, especially interstitial zinc defects in crystals [42]. Because porous ZnO particles were synthesized via a solid state reaction at relatively low temperature (500 °C), diffusion length of atoms during decomposition reaction of the precursor is relatively short. It is therefore reasonable to believe that large number of structural defects exist in the final products, which result in blue-green emission around 450 nm.

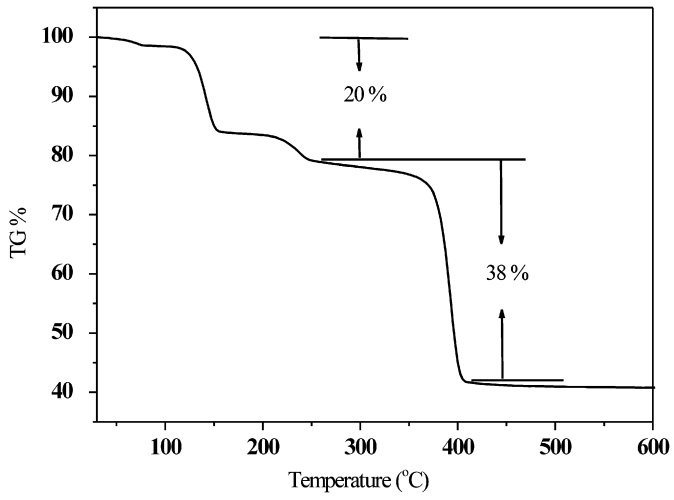

Fig. 3. TG curve for as-synthesized precursor with an octahedral shape.

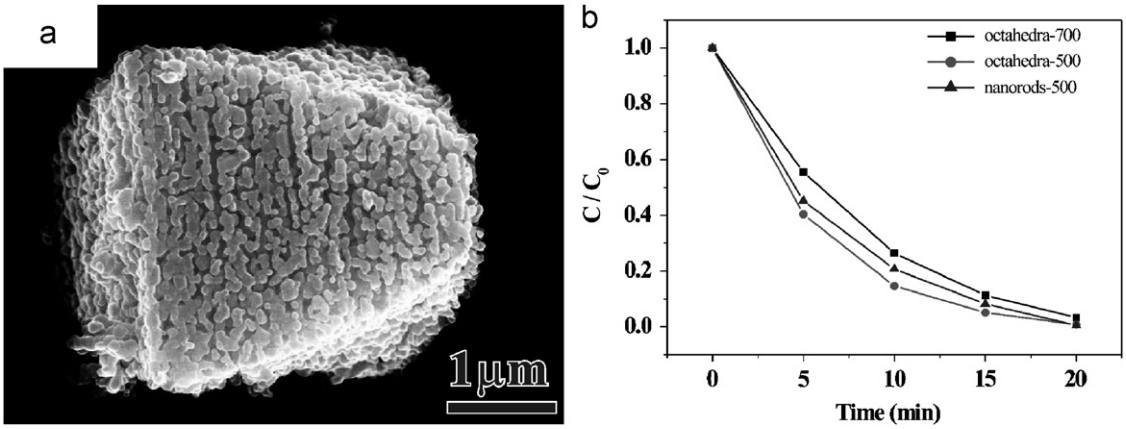

Fig. 4. (a) Typical SEM image of porous ZnO particles after a calcination at 700 °C; (b) photocatalytic degradation curves of MO as a function of the time of UV irradiation when using (●) ZnO porous octahedra calcined at 500 °C, (■) ZnO porous octahedra calcined at 700 °C, and (▲) porous ZnO nanorods calcined at 500 °C as photocatalysts.

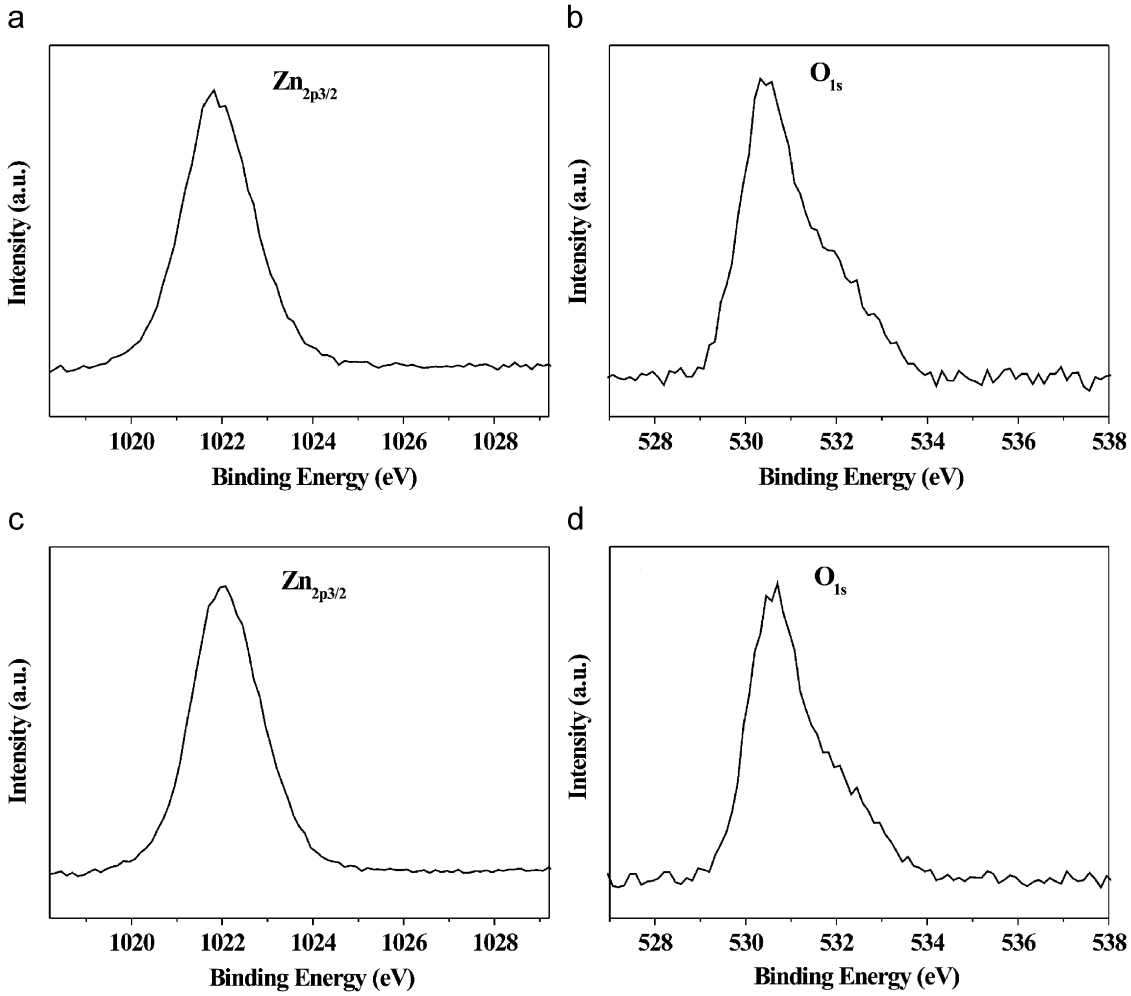

Fig. 5. (a) $Zn_{2p3/2}$ and (b) O_{1s} XPS spectra of porous ZnO octahedra (sample 1); (c) $Zn_{2p3/2}$ and (d) O_{1s} XPS spectra of porous ZnO nanorods (sample 2).

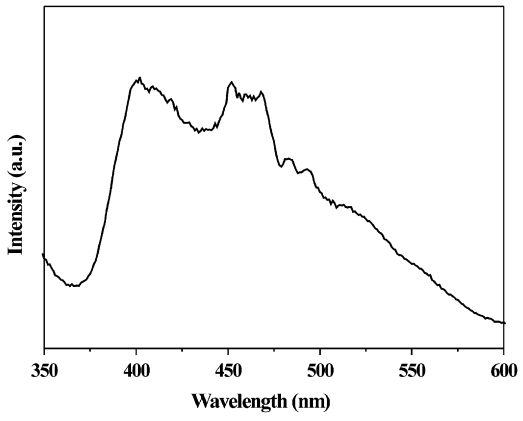

Fig. 6. Room temperature PL spectrum of as-prepared porous ZnO octahedra using an excitation wavelength of 325 nm.

4. Conclusion

In summary, two kinds of porous ZnO particles with different morphologies have been successfully fabricated via a similar synthetic process by controlling morphology of the precursors. These porous particles are constructed with numerous primary nanoparticles, and their pores originate from releasing of some gases during the calcination process of precursors. At the same time, photocatalytic studies showed that as-prepared porous ZnO particles have good photocatalytic performance due to large surface area resulting from porous structure. In principle, this synthetic route can be extended to the preparation of other metal oxide nanomaterials with porous morphologies. Therefore, the present study opens a new path toward the synthesis of porous metal oxide with special morphologies and related applications.

Acknowledgments

This work was supported by the National Natural Science Foundation of China (Grant nos. 20725310, 20721001, 20673085 and 20671078), the National Basic Research Program of China (Grant no. 2007CB815303), and Key Scientific Project of Fujian Province of China (Grant no. 2005HZ01-3).

References

[1] L. Tosheva, V.P. Valtchev, Chem. Mater. 17 (2005) 2494.
[2] H.F. Zhang, A.I. Cooper, Soft Mater. 1 (2005) 107.
[3] G. Frenzer, W.F. Maier, Annu. Rev. Mater. Res. 36 (2006) 281.
[4] I.I. Slowing, B.G. Trewyn, S. Giri, V.S.Y. Lin, Adv. Funct. Mater. 17 (2007) 1225.
[5] G.W. Nyce, J.R. Hayes, A.V. Hamza, J.H. Satcher, Chem. Mater. 19 (2007) 344.
[6] G.S. Chai, I.S. Shin, J.S. Yu, Adv. Mater. 16 (2004) 2057.
[7] J.L. Chen, C. Burger, C.V. Krishnan, B. Chu, J. Am. Chem. Soc. 127 (2005) 14140.
[8] H.L. Xu, W.Z. Wang, Angew. Chem. Int. Ed. 46 (2007) 1489.
[9] H.F. Zhang, J. Long, A.I. Cooper, J. Am. Chem. Soc. 127 (2005) 13482.
[10] W.H. Suh, K.S. Suslick, J. Am. Chem. Soc. 127 (2005) 12007.

[11] H.P. Lin, C.Y. Mou, Acc. Chem. Res. 35 (2002) 927.
[12] K. Miyasaka, L. Han, S.N. Che, O. Terasaki, Angew. Chem. Int. Ed. 45 (2006) 6516.
[13] A. Galarneau, J. Iapichella, K. Bonhomme, F.D. Renzo, P. Kooyman, O. Terasaki, F. Fajula, Adv. Funct. Mater. 16 (2006) 1657.
[14] H.M. Chen, J.H. He, H.M. Tang, C.X. Yan, Chem. Mater. 20 (2008) 5894.
[15] C.C. Yu, L.X. Zhang, J.L. Shi, J.J. Zhao, J.H. Gao, D.S. Yan, Adv. Funct. Mater. 18 (2008) 1544.
[16] Z. Guo, M.Q. Li, J.H. Liu, Nanotechnology 19 (2008) 245611.
[17] Z. Liu, P.C. Searson, J. Phys. Chem. B 110 (2006) 4318.
[18] Z.H. Dai, K. Liu, Y.W. Tang, X.D. Yang, J.C. Bao, J. Shen, J. Mater. Chem. 18 (2008) 1919.
[19] M.H. Huang, S. Mao, H. Feick, H.Q. Yan, Y.Y. Wu, H. Kind, E. Weber, R. Russo, P.D. Yang, Science 292 (2001) 1897.
[20] K. Hara, T. Horiguchi, T. Kinoshita, K. Sayama, H. Sugihara, H. Arakawa, Sol. Energy Mater. Sol. Cells 64 (2000) 115.
[21] N.J. Dayan, S.R. Sainkar, R.N. Karekar, R.C. Aiyer, Thin Solid Films 325 (1998) 254.
[22] A. Umar, M.M. Rahman, S.H. Kim, Y.B. Hahn, Chem. Commun. (2008) 166.
[23] E.S. Jang, J.H. Won, S.J. Hwang, J.H. Choy, Adv. Mater. 18 (2006) 3309.
[24] Z.L. Wang, Mater. Today June (2004) 26.
[25] H.Q. Wang, G.H. Li, L.C. Jia, G.Z. Wang, C.J. Tang, J. Phys. Chem. C 112 (2008) 11738.
[26] P.X. Gao, Z.L. Wang, J. Am. Chem. Soc. 125 (2003) 11299.
[27] B. Reeja-Jayan, E. De la Rosa, S. Sepulveda-Guzman, R.A. Rodriguez, M.J. Yacaman, J. Phys. Chem. C 112 (2008) 240.
[28] S. Bhattacharyya, A. Gedanken, Microporous Mesoporous Mater. 110 (2008) 553.
[29] J.B. Liang, S. Bai, Y.S. Zhang, M. Li, W.C. Yu, Y.T. Qian, J. Phys. Chem. C 111 (2007) 1113.
[30] C.X. Shan, Z. Liu, Z.Z. Zhang, D.Z. Shen, S.K. Hark, J. Phys. Chem. B 110 (2006) 11176.
[31] Z. Gui, J. Liu, Z.Z. Wang, L. Song, Y. Hu, W.C. Fan, D.Y. Chen, J. Phys. Chem. B 109 (2005) 1113.
[32] F.F. Wang, R.B. Liu, A.L. Pan, S.S. Xie, B.S. Zou, Mater. Lett. 61 (2007) 4459.
[33] R.Q. Song, A.W. Xu, B. Deng, Q. Li, G.Y. Chen, Adv. Funct. Mater. 17 (2007) 296.
[34] Y.L. Cao, L. Liu, D.Z. Jia, X.Q. Xin, Chin. J. Chem. 23 (2005) 539.
[35] Y.J. Zhu, W.W. Wang, R.J. Qi, X.L. Hu, Angew. Chem. Int. Ed. 43 (2004) 1410.
[36] X. Zhou, Z.X. Xie, Z.Y. Jiang, Q. Kuang, S.H. Zhang, T. Xu, R.B. Huang, L.S. Zheng, Chem. Commun. (2005) 5572.
[37] Z.Y. Jiang, T. Xu, Z.X. Xie, Z.W. Lin, X. Zhou, X. Xu, R.B. Huang, L.S. Zheng, J. Phys. Chem. B 109 (2005) 23269.
[38] C.H. Ye, Y. Bando, G.Z. Shen, D. Golberg, J. Phys. Chem. B 110 (2006) 15146.
[39] T.J. Kuo, C.N. Lin, C.L. Kuo, M.H. Huang, Chem. Mater. 19 (2007) 5143.
[40] X.L. Cao, H.B. Zeng, M. Wang, X.J. Xu, M. Fang, S.L. Ji, L.D. Zhang, J. Phys. Chem. C 112 (2008) 5267.
[41] P.T. Hsieh, Y.C. Chen, K.S. Kao, C.M. Wang, Appl. Phys. A 90 (2008) 317.
[42] K.H. Tam, C.K. Cheung, Y.H. Leung, A.B. Djurisic, C.C. Ling, C.D. Beling, S. Fung, W.M. Kwok, W.K. Chan, D.L. Phillips, J. Phys. Chem. B 110 (2006) 20865.